

Supplementary Information

Monitoring the CO₂ Enhanced Oil Recovery Process at the Nanoscale: An *In Situ* Neutron Scattering Study

Konstantinos L. Stefanopoulos,^{*a} Evangelos P. Favvas,^a Georgios N. Karanikolos,^{b,c} Waleed Alameri,^d Vassilios C. Kelessidis,^d Tristan G.A. Youngs^e and Daniel T. Bowron^e

^a Institute of Nanoscience & Nanotechnology, NCSR “Demokritos”, 153 10 Ag. Paraskevi Attikis, Athens, Greece

^b Department of Chemical Engineering, Khalifa University, P.O. Box 127788, Abu Dhabi, UAE

^c Research and Innovation Center on CO₂ and H₂ (RICH), Khalifa University, P.O. Box 127788, Abu Dhabi, UAE

^d Department of Petroleum Engineering, Khalifa University, P.O. Box 127788, Abu Dhabi, UAE

^e ISIS Neutron and Muon Source, STFC Rutherford Appleton Laboratory, Harwell Oxford, Didcot, OX11 0QX, United Kingdom

* To whom correspondence should be addressed. Email: k.stefanopoulos@inn.demokritos.gr

1. Experimental set-up for the *in situ* neutron scattering experiment

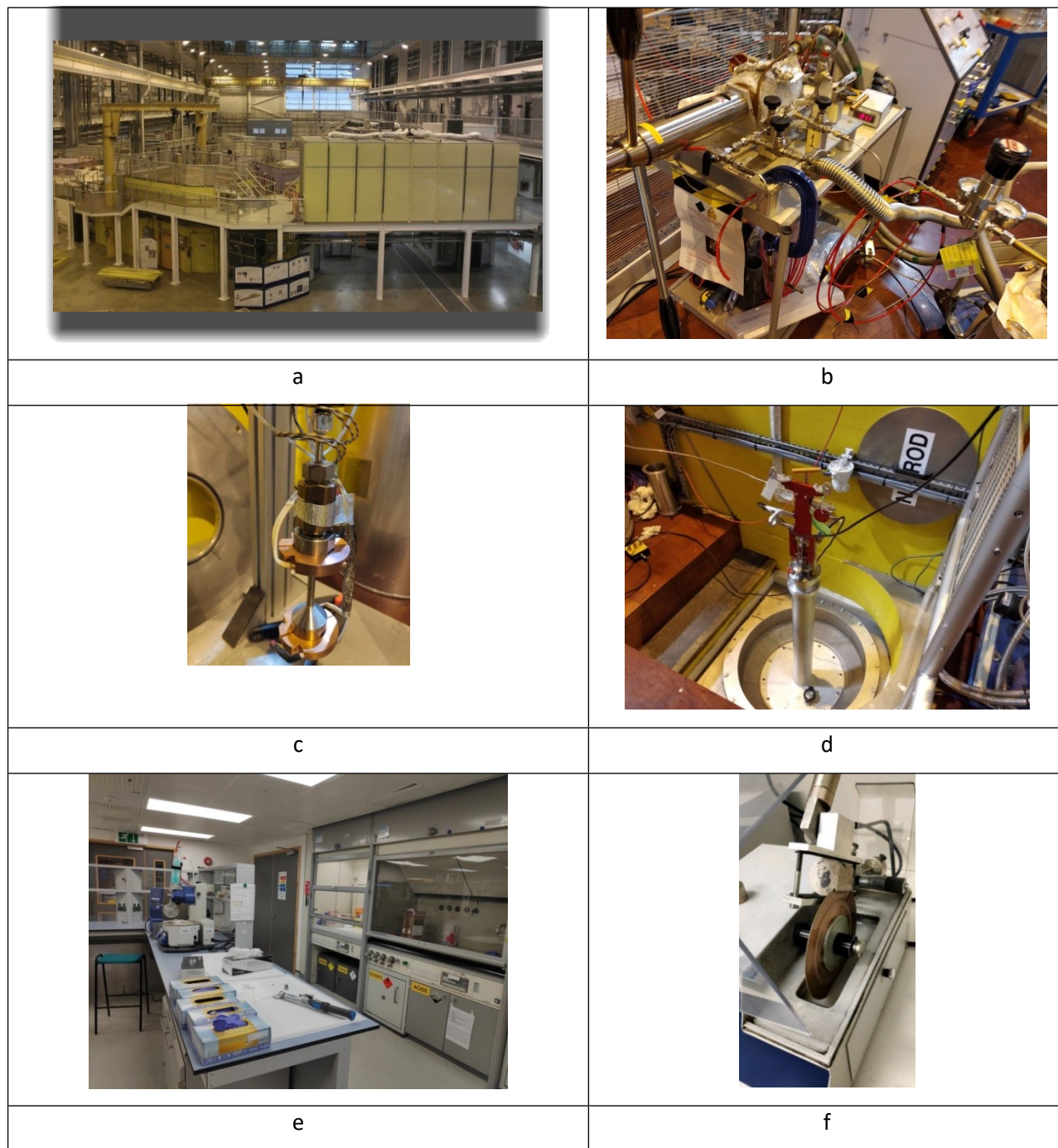


Fig. S1. (a) A view of NIMROD instrument located at Target Station 2; (b) The gas handling apparatus utilised for the *in situ* injection of pressurised supercritical CO₂ into the limestone sample. It is equipped with a pressure intensifier, a pressure transducer, a relief valve, a turbo pump, gas and vacuum connections and connected with a high-purity CO₂ cylinder; (c) The high-pressure TiZr null scattering alloy sample container with temperature control mounted on a candlestick; (d) The stick is connected to the gas handling apparatus and to the high-pressure sample container and is inserted in the neutron beam under vacuum; (e) The chemistry laboratory used for sample preparation; (f) The BRUEHLER precision cutter used for the appropriate cutting of the core samples.

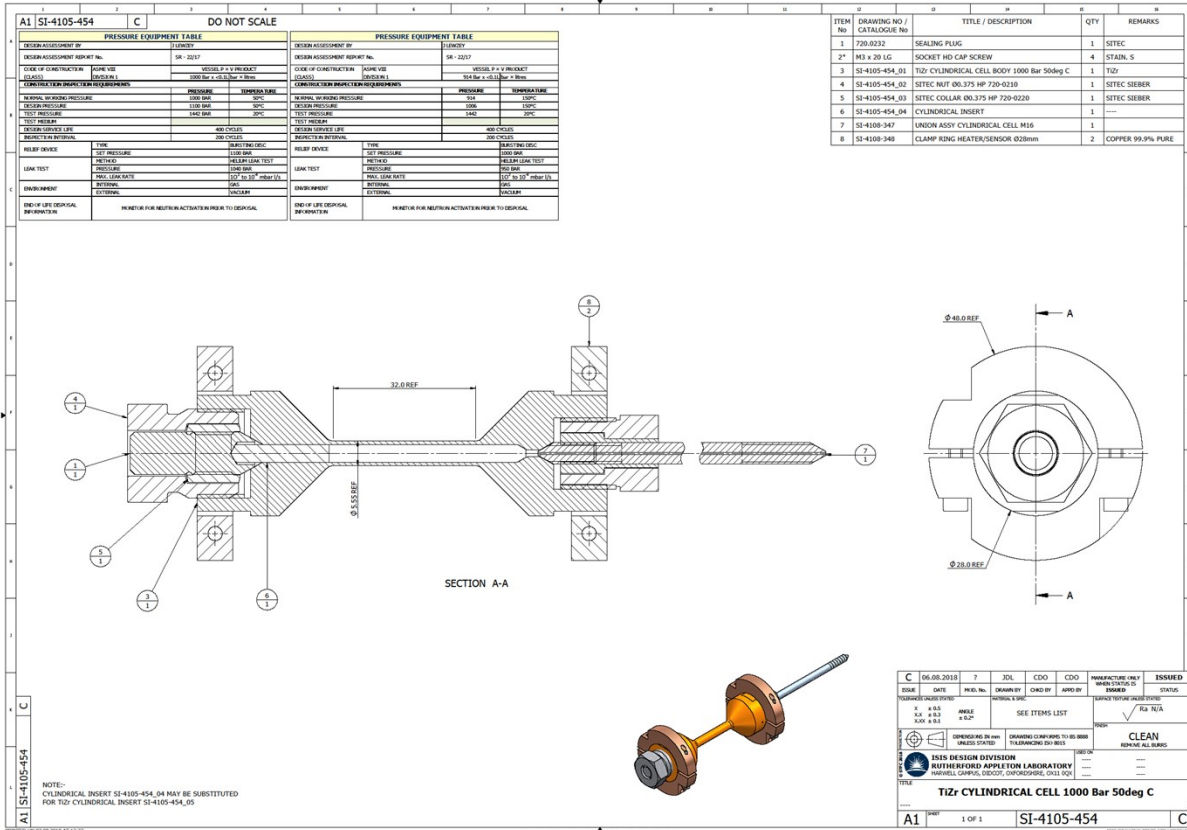


Fig. S2. Diagram of the high-pressure TiZr cell used in this study.

2. Structural details of bulk supercritical CO₂

Fig. S3a presents the total scattering factors, $S(Q)$, for the bulk supercritical CO₂ at two thermodynamic states SC1 and SC2 ($T=393$ K and pressures $P=120$ bar and $P=180$ bar, respectively). The structure factor for the bulk liquid CO₂ is also shown for comparison¹ (see also Table S1). In general, the structure factor at the low- Q region is composed of the intermolecular part (between the molecules) and the intramolecular part (within the molecule) at the high- Q regime. In case of bulk supercritical fluid, a strong scattering signal is observed at the small values of Q (intermolecular part) suggesting clustering of CO₂ molecules due to large density fluctuations. This means that the molecules are distributed in such a way that they form high-density and low-density regions.² At larger Q values, the intermolecular structure peak (main peak) is clearly visible, depending on the fluid density, d , and represents the most probable distance between the nearest-neighbour molecules. The main peak for the liquid is located at about $Q=1.80 \text{ \AA}^{-1}$ and is shifted to lower values in case of the supercritical fluid due to the reduced density (Fig. S3b, Table S1). Furthermore, the observed periodic oscillations at higher Q values arise from the strong intramolecular correlations within the molecule such as C-O and O-O (intramolecular part of the structure factor).

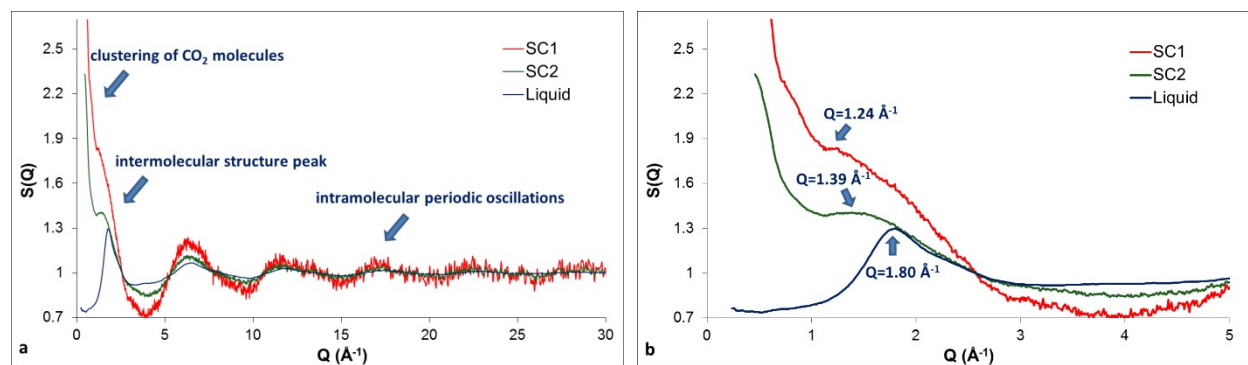
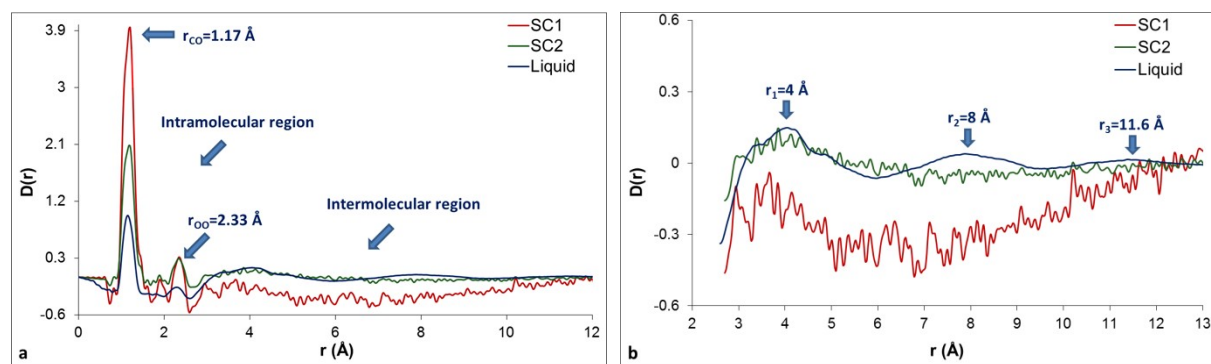


Fig. S3. The total scattering structure factor $S(Q)$ for (a) bulk supercritical CO₂ at 393 K and 120 bar (SC1) and 180 bar (SC2) respectively and for bulk liquid CO₂ at 230 K and 12 bar; (b) zoomed view of the low- Q region.

Table S1. Thermodynamic and scattering data for the bulk supercritical and liquid CO₂.

State	T (K)	P (bar)	d (g/cm ³) ³	Q_{peak} (Å ⁻¹)
SC1	393	120	0.21	1.24
SC2	393	180	0.35	1.39
liquid	230	12	1.13	1.80

Fig. S4a illustrates the total differential correlation function, $D(r)$, for the bulk supercritical (SC1 and SC2) and the bulk liquid CO₂, respectively. The two intramolecular peaks are clearly visible for both liquid and supercritical fluid at about 1.17 Å and 2.33 Å respectively and they arise from the C-O ($r_{\text{C-O}}$) and O-O ($r_{\text{O-O}}$) distances within the molecule (obviously $r_{\text{O-O}}=2r_{\text{C-O}}$). The intermolecular part of the correlation function is observed for r values larger than ~ 2.6 Å. In the case of bulk liquid, the three broad features centered at ~ 4 , ~ 8 and ~ 11.6 Å correspond respectively to the first-, second- and third-neighbour interactions (Fig. S4b). In addition a split of the first-neighbour peak into three structures is also revealed. These structures are attributed to C-C, C-O or O-O correlations arising from the CO₂ quadrupole moment.⁴ In the case of the two supercritical CO₂ states (SC1 and SC2), however, only the first-neighbour peak is observed. This result can be explained in terms of the smaller density of the supercritical fluid compared to the liquid (Table S1) resulting in both reduced short-range order and noise in the data.

**Fig. S4.** The intra- and intermolecular part of differential correlation function $D(r)$ for (a) bulk supercritical CO₂ at 393 K and 120 bar (SC1) and 180 bar (SC2) respectively and for bulk liquid CO₂ at 230 K and 12 bar; (b) zoomed view of the intermolecular region.

3. Structural details of bulk liquid deuterated n-decane (n-Decane-D22)

In general, the scattering curves for the series of liquid n-alkanes are very similar, regardless of the number of carbon atoms in the chain. In addition, the chains up to 10 carbons remain essentially straight in the liquid. To the best of our knowledge this is the first total neutron scattering measurement for n-Decane-D22. Fig. S5a shows the total scattering factor for the bulk liquid deuterated n-decane at 293 K and 1 atm. The strong main peak arises mainly from the inter-chain molecular correlations and is located at 1.34 \AA^{-1} while the following dominant oscillations are due to the first few shortest intramolecular carbon-carbon correlations.

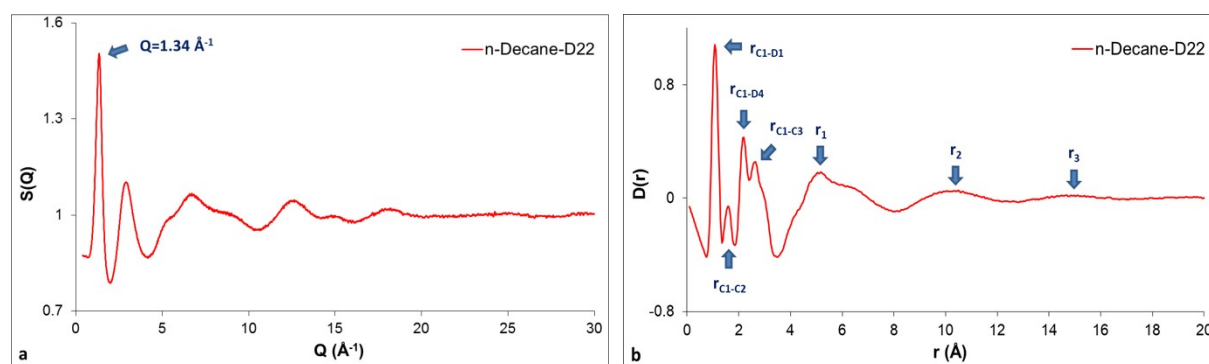


Fig. S5. (a) The total scattering structure factor $S(Q)$ and (b) the intra- and intermolecular part of differential correlation function $D(r)$ for deuterated n-decane at 293 K and 1 atm.

Fig. S5b presents the differential correlation function for the n-Decane-D22. The oscillations at small distances (up to $\sim 3.5 \text{ \AA}$) arise from the intramolecular correlations. In particular, the nearest-neighbour carbon-carbon distance (C1-C2) is 1.59 \AA while the next-nearest-neighbour distance (C1-C3) is 2.64 \AA . In addition, the carbon-deuterium bond (C1-D1) and the carbon deuterium distance on next carbon (C1-D4) have values 1.08 \AA and 2.16 \AA respectively. Finally the intermolecular peak positions corresponding to first- second- and third-neighbour correlations are located at $r_1=5.04 \text{ \AA}$, $r_2=10.47 \text{ \AA}$ and $r_3=14.97 \text{ \AA}$ respectively (see also Table S2).

Table S2. Intramolecular and intermolecular distances (Å) for n-Decane-D22 obtained from $D(r)$.

Correlation	Description	Symbol	Value
Intramolecular	Carbon-deuterium bond, C1-D1, etc.	r_{C1-D1}	1.08
Intramolecular	Carbon-carbon bond, C1-C2 etc.	r_{C1-C2}	1.59
Intramolecular	Carbon-deuterium on next carbon, C1-D4 etc.	r_{C1-D4}	2.16
Intramolecular	Carbon-next but one carbon, C1-C3 etc.	r_{C1-C3}	2.64
Intermolecular	Position of first-neighbour maximum	r_1	5.04
Intermolecular	Position of second-neighbour maximum	r_2	10.47
Intermolecular	Position of third-neighbour maximum	r_3	14.97

4. Pore accessibility to CO₂ in the limestone

A methodology has been developed for the calculation of accessible and inaccessible pore volume fraction, without the requirement of the achievement of the fluid contrast-matching pressure (or zero average contrast, ZAC), according to the following expression:⁵

$$\frac{I(P)}{I(0)} = S(P)C_{ac} + C_{in} \quad (1)$$

where $S(P) = \left[1 - \frac{\rho_f(P)}{\rho_m}\right]^2$. $I(P)$ and $I(Q)$ are the scattered intensities at fluid pressure P and at zero fluid pressure (empty pores) respectively, C_{ac} and C_{in} are the volume fractions of accessible and inaccessible pores respectively, $\rho_f(P)$ and ρ_m are the neutron scattering length densities (SLDs) of the fluid at a given pressure P and the solid matrix respectively. The gradient and the intercept of the line derived from Eq.(1) give the volume fractions of accessible and inaccessible pores at each Q value that corresponds to a definite pore radius (according to the empirical relation $Q \sim 2.5/r$). It is then possible to calculate C_{ac} or C_{in} as a function of pore radius. It is worth mentioning that the above equation has been derived by assuming that: (i) the pore morphology (i.e. the shape and size) of the accessible and inaccessible pores is similar, and (ii) there is no significant confinement of the fluid in the pores. In our present study, Eq.(1) cannot

be applied for $Q > 0.06 \text{ \AA}^{-1}$ (corresponding to pore radii $r < 41 \text{ \AA}$) mainly due to the increased CO_2 density when confined within the smaller pores.

5. Neutron profiles of dry limestone and limestone loaded with deuterated n-decane

The neutron profile of the limestone specimen with pores filled with decane differs significantly compared to that of the dry one (with empty pores). The signature of the confined decane presence is the peak located at $Q = 1.27 \text{ \AA}^{-1}$ (Fig. S6). The peak is slightly shifted to a smaller Q value compared to that of the bulk decane ($Q = 1.34 \text{ \AA}^{-1}$) (Fig. S5a). The reason of this slight peak shift is that there is a small decrease in the density of the confined phase because the neutron measurement took place at 393 K. Another striking difference is that the SANS signal arising from the limestone sample loaded with decane is reduced compared to that of the dry limestone (Fig. S6). The reason is that the neutron scattering length density (SLD) of the limestone ($\sim 4.69 \cdot 10^{-6} \text{ \AA}^{-2}$) is close to that of the deuterated decane ($6.42 \cdot 10^{-6} \text{ \AA}^{-2}$) and contrast matching is nearly fulfilled. This means that the decane presence reduces significantly the neutron scattering contrast and, thus, the scattered intensity which is proportional to the square of the contrast. However, the SANS signal is not completely vanished suggesting that the pores are not fully saturated but partially filled with decane.

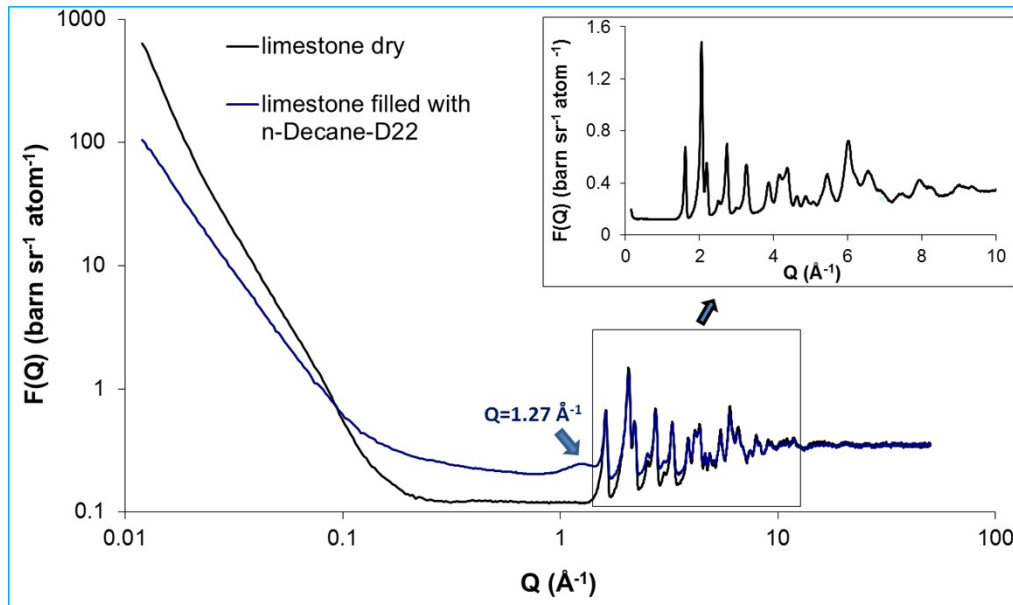


Fig. S6. Neutron scattering curves of dry limestone and limestone filled with n-Decane-D22 at 393 K. (Note the characteristic peak of n-Decane-D22 at $Q=1.27 \text{ \AA}^{-1}$). Inset: Zoomed view of the limestone diffraction pattern.

Finally, the slope of the SANS linear region of the limestone with the pores partially filled with decane is -2.5 compared to -3.2 for the dry sample with empty pores. Note that the linear regime from both samples extends along the same Q -range ($0.012\text{-}0.07 \text{ \AA}^{-1}$) corresponding to a length scale $36 \text{ \AA} - 208 \text{ \AA}$. According to SANS (or SAXS) theory⁶⁻⁷, when the power exponent is between -3 and -4 the scattering is related to surface fractals (-3 for a fractally rough and -4 for a smooth surface interface). This suggests that the power law scattering from the dry limestone sample (-3.2) is characteristic of a very rough pore-solid interface. On the other hand, when the slope is between -1 and -3 the scattering is directly related to mass fractals, i.e. objects generated by different growth processes such as cluster-cluster aggregation (aerosols), diffusion limited aggregation and percolation. In case of pore fractals, the self-similar law is obeyed by the volume of the pore empty space instead of the mass of a fractal object. It is also noteworthy that a mass (or pore) fractal with a gradient close to -1 corresponds to a more open structure while a slope close to -3 suggests a more compact structure. In case of pores filled with decane (slope: -2.5) a rather compact pore fractal structure is observed. The most probable explanation is that neutrons are almost invisible to decane because it has similar SLD with the solid matrix (limestone). If we take into account that pores are partially filled with decane, the remaining empty pore structure of the limestone seems to vary significantly compared to the completely empty one (dry limestone). This can be attributed to the fact that decane is not uniformly distributed in the complex pore network resulting in the creation of a pore fractal aggregate.

6. Minimum Miscibility pressure (MMP) of the CO₂-n-decane system

To the best of our knowledge there are few studies of MMP estimation for the CO₂-n-decane system at elevated temperatures. Mutailipu et al.⁸ calculated the interfacial tension (IFT) of CO₂ and n-decane with the Axisymmetric Drop Shape Analysis (ADSA) method at high temperatures from 298 to 373 K. Then, they estimated the MMP values by making a linear fitting of the IFTs to obtain the MMP at various temperatures (see ref. 8, Fig. 9a). Comparison of their linear

MMP fitting with other experimental results in the literature illustrates that the fitting is below the experimental measurements. We extrapolated the linear fitting to 393 K and an MMP value of 148 bar was deduced. Nagarajan et al.⁹ and Reamer et al.¹⁰ have carried out experimental vapour-liquid equilibrium phase compositions, phase densities, and interfacial tensions for the CO₂-n-decane system. They both measured an MMP value of 164 bar at 377 K. In addition, Reamer et al.¹⁰ have extracted an MMP value of 186 bar at 411 K.

References

1. K. L. Stefanopoulos, F. K. Katsaros, T. A. Steriotis, A. A. Sapalidis, M. Thommes, D. T. Bowron and T. G. A. Youngs, Anomalous Depletion of Pore-Confined Carbon Dioxide upon Cooling below the Bulk Triple Point: An in Situ Neutron Diffraction Study, *Phys. Rev. Lett.*, 2016, **116**, 025502.
2. R. Ishii, S. Okazaki, I. Okada, M. Furusaka, N. Watanabe, M. Misawa and T. Fukunaga, A structural study of supercritical Xe, CO₂, and CF₃Cl by neutron scattering measurements, *Mol. Phys.*, 1998, **95**, 43-49.
3. E. Lemmon, M. McLinden and D. Friend, Thermophysical properties of fluid systems, NIST Chemistry webbook, NIST Standard reference database, 69, National Institute of Standards and Technology, Gaithersburg MD, 20899, USA, <https://webbook.nist.gov/chemistry/fluid/> (accessed September, 2021).
4. S. Chiappini, M. Nardone and F. P. Ricci, Neutron diffraction measurements on high pressure supercritical CO₂, *Mol. Phys.*, 1996, **89**, 975-987.
5. J. Bahadur, C. R. Medina, L. He, Y. B. Melnichenko, J. A. Rupp, T. P. Blach and D. F. R. Mildner, Determination of closed porosity in rocks by small-angle neutron scattering, *J. Appl. Cryst.*, 2016, **49**, 2021–2030.
6. Y. B. Melnichenko. *Small-angle scattering from confined and interfacial fluids: Applications to energy storage and environmental science* (Springer, 2015).
7. R. Zhang, S. Liu and Y. Wang, Fractal evolution under *in situ* pressure and sorption conditions for coal and shale, *Scientific Reports*, 2017, **7**, 8971.
8. M. Mutailipu, L. Jiang, X. Liu, Y. Liu and J. Zhao, CO₂ and alkane minimum miscible pressure estimation by the extrapolation of interfacial tension, *Fluid Ph. Equilibria*, 2019, **494**, 103-114.
9. N. Nagarajan and R. L. Robinson Jr., Equilibrium phase compositions, phase densities, and interfacial tensions for carbon dioxide + hydrocarbon systems. 3. CO₂ + cyclohexane. 4. CO₂ + benzene, *Chem. Eng. Data*, 1986, **31**, 168-171.
10. H. H. Reamer and B. H. Sage, Phase Equilibria in Hydrocarbon Systems. Volumetric and Phase Behavior of the n-Decane-CO₂ System, *Chem. Eng. Data*, 1963, **8**, 508-513.